The final publication is available at Springer via http://dx.doi.org/10.1007/s00348-017-2335-9

PIV-based estimation of unsteady loads on a flat plate at high angle of attack using momentum equation approaches

A. Guissart · L.P. Bernal · G. Dimitriadis · V.E. Terrapon

Abstract This work presents, compares and discusses results obtained with two indirect methods for the calculation of aerodynamic forces and pitching moment from 2D Particle Image Velocimetry (PIV) measurements. Both methodologies are based on formulations of the momentum balance: the integral Navier-Stokes equations and the "flux equation" proposed by Noca et al. (1999), which has been extended to the computation of moments. The indirect methods are applied to spatio-temporal data for different separated flows around a plate with a 16:1 chord-to-thickness ratio. Experimental data are obtained in a water channel for both a plate undergoing a large amplitude imposed pitching motion and a static plate at high angle of attack. In addition to PIV data, direct measurements of aerodynamic loads are carried out to assess the quality of the indirect calculations. It is found that indirect methods are able to compute the mean and the temporal evolution of the loads for two-dimensional flows with a reasonable accuracy. Nonetheless, both methodologies are noise sensitive and, the parameters impacting the computation should thus be chosen carefully. It is also shown that results can be improved through the use of Dynamic Mode Decomposition (DMD) as a pre-processing step.

A. Guissart · G. Dimitriadis · V.E. Terrapon
Department of Aerospace and Mechanical Engineering
University of Liege, Liège, Belgium
Tel.: +32 (0)4 366 9197
E-mail: amandine.guissart@ulg.ac.be

L.P. Bernal
Department of Aerospace Engineering
University of Michigan, Ann Arbor, Michigan, USA

1 Introduction and motivation

Aerodynamic forces and moments are conventionally measured by means of a load balance. However, this approach has some limitations, such as high relative errors for small aerodynamic loads. Moreover, when the body is moving, these devices measure not only the aerodynamic forces and moments but also the structural response which contaminates the measurements (Rival et al., 2009). For such cases, another option is to calculate the loads directly from the flow field. This calculation can be performed by using pressure sensitive paint (McLachlan and Bell, 1995), Pitot tube wake rakes (Jones, 1936) or pressure taps (Tropea et al., 2007). Although these approaches have been proven to be reliable and accurate, they also have limitations. Their accuracy can decrease with decreasing airspeed, they can be affected by zero drifting in time, they can be limited in frequency sampling or they have an intrusive effect, disturbing the flow (Tropea et al., 2007; Barlow et al., 1999). An interesting alternative to these methods is to use Particle Image Velocimetry (PIV) (Adrian, 1991; Raffel et al., 2013) velocity fields to indirectly calculate the aerodynamic loads.

A first methodology was proposed by Lin and Rockwell (1996) who used the vorticity field computed from PIV data to estimate the instantaneous lift. As the method requires the knowledge of the entire vorticity history, the PIV window should theoretically be infinite if the vorticity is convected by the flow. Lin and Rockwell (1996) circumvented this limitation by applying the formulation to an oscillating cylinder in a still fluid, so that the vorticity remained confined in a finite domain that could be captured by the PIV window.

The method was then extended by Noca et al. (1997) to eliminate the domain size limitation. Derived from

the integral form of the momentum equation applied to a control surface surrounding the geometry of interest, his formulation expresses the forces solely in terms of the velocity field and its derivatives by re-writing the pressure term. This approach requires an accurate evaluation of the vorticity on the entire control surface, including the region near the body. However, obtaining the velocity field in the vicinity of geometries, especially moving ones, can be challenging due to reflections of the laser sheet. To overcome this drawback, Noca et al. (1999) proposed alternative approaches, where the knowledge of the velocity and vorticity fields are required only on the contours of the control surface. These formulations were used by Tan et al. (2005) to compute the instantaneous forces on a cylinder. More recently, Sterenborg et al. (2014) used the same methodology to estimate the unsteady loads on an airfoil with an actuated flap.

In parallel to the work of Noca et al. (1999), Unal et al. (1997) showed that the classical integral form of the momentum equation can be directly used to estimate the loads on a body. In this case both contour and surface integrals of the velocity and pressure fields are required. Nonetheless, the pressure can be obtained from the PIV data through the application of the Navier-Stokes equations. This methodology has been applied to numerous cases (van Oudheusden et al., 2006; Kurtulus et al., 2007; Gharali and Johnson, 2014; Villegas and Diez, 2014).

In the present work, the so-called "flux equation" proposed by Noca et al. (1999) and the integral form of the Navier-Stokes equations are applied to spatio-temporal data obtained for the flow around a static or pitching flat plate. The former has been here extended to the calculation of moments since the original "flux equation" of Noca et al. (1999) had only been formulated for forces. Although these approaches are outwardly simple, several difficulties must be overcome to ensure accurate results. First, the velocity cannot be measured in shadow regions inherent to most PIV setups, thus preventing the straightforward application of the control volume approach. In the context of this work, the missing data points are found by leveraging the symmetry of the problem. As mentioned above, another challenge of the methodology based on the integral formulation of the Navier-Stokes equations stems from the fact that PIV measurements do not provide the pressure field. Therefore, it must be indirectly determined from the velocity field. This can be achieved by either integrating the pressure gradient calculated from the velocity field through the Navier-Stokes equations or by solving the pressure Poisson equation, as detailed in the review paper of van Oudheusden (2013). The latter approach has been used in several studies which focus on the pressure field calculation from PIV (Gurka et al., 1999; Dabiri et al., 2014; Laskari et al., 2016). In the present work the pressure is required only along a contour so that the former method is less costly and has thus been chosen here.

As shown by David et al. (2009) and Gharali and Johnson (2014), the velocity noise impacts the accuracy of the pressure calculation and thus of the force estimation. Moreover, the quality of the results is also affected by different parameters such as the location and size of the PIV window, the spatio-temporal resolution (David et al., 2009; Albrecht et al., 2013; Gharali and Johnson, 2014) or the type of flow. The present work aims to extend these results by considering two different PIV-based indirect load calculations and by investigating the effect of several parameters. In particular, it analyses the aerodynamic loads, including the pitching moment, for the flow around a flat plate in different configurations. First, a large-amplitude pitching motion is imposed and three pivot axes are considered. Note that this case is closely related to the work of Gharali and Johnson (2014) who studied the dynamic stall of an airfoil. In a second step, the flow around a static plate at different angles of attack is analyzed, a case also studied by Albrecht et al. (2013). Finally, aerodynamic forces and moment obtained by the two indirect methods are assessed by comparison to direct measurements with a load balance.

This article is organized as follows. Section 2 summarizes the mathematical background of the indirect calculation methods and their implementation. It also discusses different sources of error and proposes some improvement strategies. Section 3 describes the specific applications considered and the experimental procedure. The results of the indirect load calculations and the comparison with direct measurements are then shown and discussed in Sect. 4. Finally, conclusions and future work are presented in Sect. 5.

2 Methodology

This section describes the mathematical formulation for both methodologies based on the integral Navier-Stokes equations (INSE) and the "flux equation" proposed by Noca et al. (1999) (NOCA). The calculation of the pressure required by the first method is also detailed and the implementation of both methods is explained. Finally, Dynamic Mode Decomposition (DMD) is introduced as a possible strategy for improving the quality of the results.

2.1 Indirect load calculations

The flows studied in this work being turbulent, only statistical mean fields are considered (denoted by $\overline{\cdot}$). In this context, averaging the different equations appearing in both the INSE and NOCA methods introduces a new term, the Reynolds stress tensor $\overline{u_i' u_j'}$ (where $\cdot'$ denotes fluctuations around the mean). Furthermore, as the velocity field is obtained from 2D-PIV measurements at low Mach number, only the two-dimensional incompressible case is considered.

2.1.1 Load calculation based on the INSE *formulation*

The indirect calculation of the aerodynamic forces and moment is here based on the integral form of the Navier-Stokes equations applied to a control surface $\mathcal{S}$ defined by an external contour $\mathcal{C}_\infty$ surrounding the geometry of interest (Unal et al., 1997). The average aerodynamic force vector is expressed as

$$\begin{aligned}\overline{F}_i = &- \mathrm{d}_t \int_{\mathcal{S}} \rho \overline{u}_i \, \mathrm{d}\mathcal{S} - \oint_{\mathcal{C}_\infty} \overline{p} n_i \, \mathrm{d}\mathcal{C} \\ &+ \oint_{\mathcal{C}_\infty} \left(-\rho \overline{u}_i \overline{u}_j + \overline{\tau}_{ij} - \rho \overline{u_i' u_j'} \right) n_j \, \mathrm{d}\mathcal{C},\end{aligned} \tag{1}$$

and the pitching moment $\overline{M}_z$ about point R, defined positive nose up, is

$$\begin{aligned}\overline{M}_z = &- \mathrm{d}_t \int_{\mathcal{S}} \rho \overline{u}_i r_k \epsilon_{ik} \, \mathrm{d}\mathcal{S} - \oint_{\mathcal{C}_\infty} \overline{p} n_i r_k \epsilon_{ik} \, \mathrm{d}\mathcal{C} \\ &+ \oint_{\mathcal{C}_\infty} \left(-\rho \overline{u}_i \overline{u}_j + \overline{\tau}_{ij} - \rho \overline{u_i' u_j'} \right) n_j r_k \epsilon_{ik} \, \mathrm{d}\mathcal{C},\end{aligned} \tag{2}$$

where ρ is the constant density, $\overline{u}_i$ the average velocity vector, $\overline{p}$ the average pressure, $\overline{\tau}_{ij}$ the average viscous stress tensor, r_i the location vector with respect to point R and ϵ_{ij} is the two-dimensional Levi-Civita symbol. The above expressions contain both surface integrals over the control surface $\mathcal{S}$ and closed-path integrals along its external contour $\mathcal{C}_\infty$. The vector n_i represents the unit outward vector normal to the contour. A schematic of the configuration is shown in Fig. 1.

Each term in the above expression can be calculated from the average velocity field $\overline{u}_i$ obtained from PIV measurements. In particular, the average viscous stress tensor $\overline{\tau}_{ij}$ is computed from the average velocity gradient

$$\overline{\tau}_{ij} = \mu \left(\partial_i \overline{u}_j + \partial_j \overline{u}_i \right), \tag{3}$$

where the dynamic viscosity μ is constant. The average pressure field $\overline{p}$ is generally unknown but can also be derived from the average velocity field. Two approaches can be considered, both based on the knowledge of the average pressure derivatives calculated by using the averaged Navier-Stokes equations:

$$\partial_i \overline{p} = -\rho \partial_t \overline{u}_i - \rho \overline{u}_j \partial_j \overline{u}_i + \mu \partial^2_{jj} \overline{u}_i - \partial_j \overline{u_j' u_i'}. \tag{4}$$

The first option is to solve the Poisson equation obtained by taking the divergence of Eq. (4). Boundary conditions of Neumann type can be applied by using Eq. (4). The second option consists in integrating along $\mathcal{C}_\infty$ the component of the pressure gradient $\partial_i \overline{p}$ that is tangential to the contour. Because the use of the pressure Poisson equation increases the computational time without improving results significantly (Albrecht et al., 2012), the second option has been chosen here. Since the integration path is closed, the average pressure computed at the last point E (see Fig. 1) should be equal to the initial value at point A, i.e., $\overline{p}_\mathrm{E} = \overline{p}_\mathrm{A} = \overline{p}_\mathrm{init}$. In practice, a discrepancy between these two values is typically observed because the PIV data are only available at discrete points and entail measurement errors. Nonetheless, the integration error $\varepsilon_{\overline{p}} = \overline{p}_\mathrm{A} - \overline{p}_\mathrm{E}$ can be used to improve the pressure calculation.

The approach used here is based on the one proposed by Kurtulus et al. (2007), who estimated the pressure from the Bernoulli equation outside the viscous wake (segments A-B-B′ and C′-C-D-E in Fig. 1) and integrated Eq. (4) in the wake region (segment B′-C′). The value obtained in C′ was then compared to the one computed from the Bernoulli equation and the discrepancy was redistributed with a linear weighting along B′-C′. Here, Eq. (4) is used along the entire contour $\mathcal{C}_\infty$ but the correction is only applied in the wake region. The assumption that most of the error is generated in the wake (and then simply propagated along the rest of the contour) seems reasonable since the edge B-C is the zone where the spatio-temporal variations of the velocity and pressure are the largest, and, thus, the numerical integration of the pressure gradient is the most challenging. Based on this assumption, the error $\varepsilon_{\overline{p}}$ is simply removed from the computed value $\overline{p}$ along edges E-D-C-C′. Similarly to Kurtulus et al. (2007), it is assumed that the error $\varepsilon_{\overline{p}}$ increases linearly in the wake (segment B′-C′) and the pressure is corrected accordingly. The wake is here defined as the region of large-scale vorticity. In the context of this work, it is identified by the Γ_2 function (Graftieaux et al., 2001) which provides the location of the large-scale vortex boundary based on the topology of the velocity field. This method was preferred to the one based on the vorticity proposed by Kurtulus et al. (2007), as the velocity field is less noisy than its spatial derivatives. The value of the Γ_2 function at a point P on the boundary

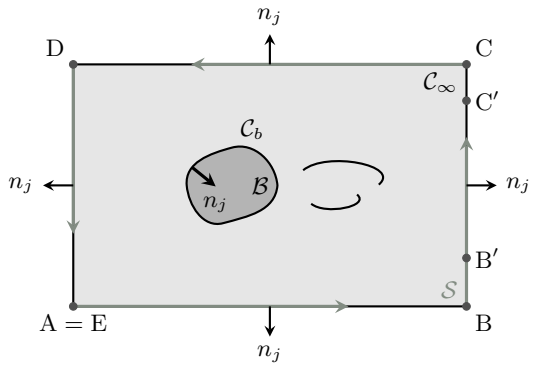

Fig. 1: Schematic view of the control surface $\mathcal{S}$ and its contours $\mathcal{C}_\infty$ and $\mathcal{C}_b$ around the geometry $\mathcal{B}$ of interest

is given by the integral over a small area A around P

$$\Gamma_2 = \frac{1}{A}\int_{\mathrm{M}\in A} \frac{\left[(\mathbf{x}^{\mathrm{M}}-\mathbf{x}^{\mathrm{P}})\times\left(\mathbf{u}^{\mathrm{M}}-\tilde{\mathbf{u}}^{\mathrm{P}}\right)\right]\cdot\mathbf{e}_z}{\|(\mathbf{x}^{\mathrm{M}}-\mathbf{x}^{\mathrm{P}})\|\|\mathbf{u}^{\mathrm{M}}-\tilde{\mathbf{u}}^{\mathrm{P}}\|}\,\mathrm{d}A, \quad (5)$$

where $\mathbf{x}^{\mathrm{M}}$ is the location of a point M that lies on the surface A, and $\mathbf{e}_z$ is the unit vector normal to the measurement plane. Finally, $\mathbf{u}^{\mathrm{M}}$ is the velocity vector associated to M and $\tilde{\mathbf{u}}^{\mathrm{P}}$ is a local convection velocity around P defined as $\tilde{\mathbf{u}}^{\mathrm{P}} = {}^1\!/_A\int_A \mathbf{u}\,\mathrm{d}A$. The Γ_2 function is computed for each point along the edge B-C. The wake is then identified as the region for which $\|\Gamma_2\| > \Gamma_2^{\mathtt{thres}}$, where $\Gamma_2^{\mathtt{thres}}$ is a threshold value to be chosen.

To summarize, the pressure $\overline{p}$ is obtained in two steps: first, the pressure is computed on $\mathcal{C}_\infty$ by integrating the pressure gradient from A to E and by calculating the error $\varepsilon_{\overline{p}}$. Then the pressure distribution on edge B-C is corrected in three steps: on C′-C, the error $\varepsilon_{\overline{p}}$ is removed from the initially computed pressure; on B′-C′, $\varepsilon_{\overline{p}}$ is removed linearly; and on B-B′, the initially calculated pressure is not corrected.

2.1.2 Load calculation based on the NOCA *formulation*

In addition to the methodology described above, the forces and pitching moment are also indirectly calculated by using one of the formulations proposed by Noca et al. (1999). In particular, the present work uses the two-dimensional version of the "flux equation" with which forces expresses the forces as

$$\begin{aligned}\overline{F}_i = &\oint_{\mathcal{C}_\infty}\left(\overline{\gamma}_{ji}^{Ft}+\overline{\gamma}_{ji}^{Fp}-\rho\overline{u}_j\overline{u}_i+\overline{\tau}_{ji}-\rho\overline{u_j'u_i'}\right)n_j\,\mathrm{d}\mathcal{C}\\ &-\mathrm{d}_t\oint_{\mathcal{C}_b}\rho n_j\overline{u}_j x_i\,\mathrm{d}\mathcal{C},\end{aligned} \quad (6)$$

where tensors $\overline{\gamma}_{ij}^{Ft}$ and $\overline{\gamma}_{ij}^{Fp}$ are defined as

$$\begin{aligned}\overline{\gamma}_{ij}^{Ft} = &-\rho\partial_t\overline{u}_i x_j,\\ \overline{\gamma}_{ij}^{Fp} = &-\rho\overline{u}_i x_k\overline{\omega}_z\epsilon_{jk}+\frac{\rho}{2}\overline{u}_k\overline{u}_k\delta_{ij}+\rho x_i\partial_t\overline{u}_j\\ &-\rho x_k\partial_t\overline{u}_k\delta_{ij}+x_l\partial_k\overline{\tau}_{kl}\delta_{ij}-x_i\partial_k\overline{\tau}_{kj}\\ &+\rho x_i\partial_k\overline{u_k'u_j'}-\rho x_l\partial_k\overline{u_k'u_l'}\delta_{ij}.\end{aligned} \quad (7)$$

In Eqs. (6)-(7), x_i is a location vector with respect to an arbitrarily defined origin, $\mathcal{C}_b$ is the closed-path defining the body boundary as shown in Fig. 1, δ_{ij} is the Kronecker delta, and $\overline{\omega}_z$ is the average vorticity which can be obtained from the average velocity gradient as

$$\overline{\omega}_z = \partial_l\overline{u}_m\epsilon_{lm}. \quad (8)$$

This formulation can be derived from the Navier-Stokes momentum integral equations, where $\overline{\gamma}_{ij}^{Fp}$ represents the pressure contribution, while the sum of $\overline{\gamma}_{ij}^{Ft}$ and the last integral in Eq. (6) corresponds to the temporal term. Note that unlike Eq. (1), Eq. (6) enables the calculation of loads by using only closed-path integrals and does not need the knowledge of pressure. Finally, the last term in Eq. (6) requires the spatio-temporal evolution of the body location. This can be difficult to obtain directly from PIV measurements due to reflections appearing near the surface. Nonetheless, in cases of rigid body motions, these terms can be directly expressed in terms of the overall body kinematics (Noca et al., 1999). The body displacement can be decomposed into a rigid translation at velocity u_i^t and rotation around axis z at angular velocity $\dot{\alpha}_z^r$ (defined positive clockwise). The body motion is then

$$u_i^b = u_i^t - \dot{\alpha}_z^r\left(x_k^r - x_k\right)\epsilon_{ik}, \quad (9)$$

where x_i^r is the position of the center of rotation. Finally, the integral along $\mathcal{C}_b$ in Eq. (6) can be re-written as

$$-\mathrm{d}_t\oint_{\mathcal{C}_b}\rho n_j\overline{u}_j x_i\,\mathrm{d}\mathcal{C} = \rho\mathcal{B}\mathrm{d}_t u_i^t + \rho\mathcal{B}\overline{x}_j^r\mathrm{d}_t\dot{\alpha}^r\epsilon_{ij}, \quad (10)$$

where $\mathcal{B}$ is the area of the body profile, and $\overline{x}_i^r$ the location vector of the body's centroid defined with respect to the pivot point. The term requiring the spatio-temporal evolution of the body location is thus calculated from the known kinematics without using PIV measurements.

Starting from Eq. (2), a similar formulation to the one described by Eqs. (6)-(7) can be derived for the calculation of moment (the reader can find the complete derivation in App. A). Similarly to the forces, the moment can be expressed solely in terms of contour integrals. However, the rewriting of the temporal term

consists partly of an integral along the body surface involving the vorticity (see App. A), which is very difficult to compute accurately from PIV data. In this context, it is better to keep the temporal term as a surface integral. Therefore, the pitching moment around R is here calculated by rewriting only the pressure term and is expressed as

$$\begin{aligned}\overline{M}_z = &- \mathrm{d}_t \int_{\mathcal{S}} \rho \overline{u}_i x_k \epsilon_{ik} \, \mathrm{d}\mathcal{S} + \oint_{\mathcal{C}_\infty} n_i \overline{\gamma}_i^{Mp} \, \mathrm{d}\mathcal{C} \\ &+ \oint_{\mathcal{C}_\infty} \left(-\rho \overline{u}_i \overline{u}_j + \overline{\tau}_{ij} - \rho \overline{u_i' u_j'} \right) n_j x_k \epsilon_{ik} \, \mathrm{d}\mathcal{C},\end{aligned} \tag{11}$$

where the vector $\overline{\gamma}_i^{Mp}$ represents the pressure contribution and is defined as

$$\begin{aligned}\overline{\gamma}_i^{Mp} = &- \frac{\rho}{2} x_k x_k \partial_t \overline{u}_j \epsilon_{ij} - \frac{\rho}{2} x_k x_k \overline{\omega}_z \overline{u}_i \\ &+ \frac{\rho}{2} \overline{u}_k \overline{u}_k x_j \epsilon_{ij} + \frac{1}{2} x_k x_k \partial_l \overline{\tau}_{lj} \epsilon_{ij} \\ &- \frac{\rho}{2} x_k x_k \partial_l \overline{u_l' u_j'} \epsilon_{ij}.\end{aligned} \tag{12}$$

Note that the origin must be defined at point R, so that $r_i = x_i$. To estimate the pitching moment about a different point, the contribution of forces calculated by Eq. (6) have to be added to the value provided by Eq. (11).

2.2 Implementation

The different formulations must be discretized in order to be applied to discrete PIV data. For both INSE and NOCA methods, spatial derivatives are only required along the contour $\mathcal{C}_\infty$. They are calculated by using central finite difference schemes of fourth order for the first spatial derivatives and of second order for the second spatial derivatives. The temporal derivatives $\partial_t \overline{u}_i$ appearing in the NOCA methodology are computed with a fourth order central scheme.

The average pressure needed for the INSE methodology is calculated by integrating the average pressure gradient obtained from Eq. (4) along the closed path $\mathcal{C}_\infty$ as illustrated in Fig. 1. The integration path starts at point A where the pressure is chosen to be $\overline{p}_{init}$ and goes along $\mathcal{C}_\infty$ counterclockwise until point E = A. For each of the N points, a relation between the pressure and its derivatives can be written by using a finite difference scheme. To avoid an odd-even decoupling, a non-symmetric third order scheme is used for all points except the corners A, B, C, D and E, where a third order forward/backward scheme is used. This discretization can be expressed as a system of N equations that is solved for the N unknown pressure values. Once this system is solved, the pressure is corrected according to the methodology described in Sect. 2.1.1, the correction requiring the knowledge of the function Γ_2 on edge B-C. To be more general, Γ_2 is calculated on the entire surface $\mathcal{S}$ by applying Eq. (5) in which A is a square of length l. It has been demonstrated that length l has no significant impact on vortex detection (Graftieaux et al., 2001).

Finally, the integrations on the contour $\mathcal{C}_\infty$ and surface $\mathcal{S}$ appearing in Eqs. (1), (2), (6) and (11) are performed by using the rectangle rule.

2.3 Removing noise by using DMD

Results can be improved through a pre-processing step that decreases the noise level in measurements. This was shown by Charonko et al. (2010) who used Proper Orthogonal Decomposition (POD) to improve the estimation of the pressure field obtained from PIV. Alternatively, a DMD approach can be used. In this case, the spatio-temporal data is decomposed into spatial modes $\boldsymbol{\phi}_i$ oscillating at a single complex frequency λ_i with corresponding initial amplitude a_i (Schmid, 2010). The original data $\mathbf{f}(x, y, t)$ can thus be written as

$$\mathbf{f}(x, y, t) = \sum_{k=1}^{K} a_k \boldsymbol{\phi}_k (x, y) \exp(\lambda_k t), \tag{13}$$

where K is the total number of modes. To decrease the noise in $\overline{u}_i$ and $\overline{u_i' u_j'}$, these quantities are first decomposed by using DMD. The modes are then sorted with respect to their initial amplitude a_k and only the first few modes are used to reconstruct the fields. In other words, the sum in Eq. (13) is truncated, keeping only the most significant modes. The reconstructed fields are therefore only an approximation of the initial fields. They are used here to compute the aerodynamic loads.

The accuracy of this reconstruction depends not only on the number of modes used but also on the complexity of the initial data. As the flow considered here is expected to be periodic with a few dominant frequencies/modes corresponding to the shedding/pitching frequency and its harmonics, a few modes should be sufficient to obtain a good approximation. Note that the spatio-temporal resolution of the initial data should be high enough to obtain relevant modes.

3 Flow configurations and experimental setup

The two indirect load calculation methods are applied to three different cases of unsteady flow around a plate.

As large angles of attack are considered, the flow is massively separated and unsteady, which represents a major challenge for the indirect methods. The three cases and their specificities are first discussed. In a second step, the experimental setup is described.

3.1 Description of the different cases

The first case considers a forced pitching oscillation with a large amplitude. The objective is to assess the ability of the indirect methods to deal with moving bodies. A sinusoidal pitching motion $\alpha = \overline{\alpha} + \Delta\alpha \sin(2\pi f t)$ is imposed, with a mean angle of attack $\overline{\alpha} = 0^\circ$ and an amplitude $\Delta\alpha = 30^\circ$. The reduced frequency $k = \pi f c / U_\infty$ is 0.2 corresponding to the maximal reduced frequency studied by Sterenborg et al. (2014). Three pivot axes are considered: at mid-chord and at the leading and trailing edges. The Reynolds number is $\mathrm{Re} = U_\infty c/\nu = 2 \cdot 10^4$, where U_∞ is the freestream velocity, and ν the kinematic viscosity. The imposed pitching is used to synchronize the PIV apparatus with the motion of the plate so that several PIV frames can be obtained at the same specific phase of the motion. Consequently, the velocity field can be phase-averaged.

The second case corresponds to a static plate at two different angles of attack, 30° and 45°, and a Reynolds number $\mathrm{Re} = 4 \cdot 10^4$. As the shedding is not perfectly periodic, it cannot be used to synchronize the PIV system. Moreover, the sampling frequency of the apparatus is too low to ensure a sufficient resolution for a single cycle. Therefore, only the mean flow is considered here. The objective is to assess whether the indirect load calculations are able to predict the mean aerodynamic coefficients based on the mean velocity field. More specifically, in this particular case, the averaging operation in INSE and NOCA formulations can be understood as time-averaging, or more precisely an ensemble average over all PIV fields.

The third case attempts to alleviate the lack of reference for phase-averaging by forcing the periodic shedding at a given frequency. To this end, a sinusoidal pitching motion $\alpha = \overline{\alpha} + \Delta\alpha \sin(2\pi f t)$ with a very small amplitude $\Delta\alpha$ is imposed around the mean angle of attack $\overline{\alpha}$. The pivot axis is located at the center of the plate and the frequency is chosen to be as close as possible to the mean shedding frequency of the static plate. The PIV system can then be synchronized with the forcing frequency without strong alteration of the natural flow dynamics compared to the static plate (Lam and Leung, 2005). PIV velocity fields can therefore be obtained at selected phases and phase-averaging can be applied to analyze the time response of the velocity field and aerodynamic forces and moment within a cycle. Here again the Reynolds number is $\mathrm{Re} = 4 \cdot 10^4$ and both 30° and 45° are used as mean angles of attack. The imposed amplitude $\Delta\alpha$ around the mean angle is 0.77° for the lowest mean incidence and 1.33° for the highest. In both cases, the non-dimensional frequency, i.e., the Strouhal number, $\mathrm{St} = fc \sin\overline{\alpha}/U_\infty$ is 0.155, where f is the forcing frequency.

3.2 Experimental setup

The different experimental measurements are conducted in the low-turbulence free-surface water channel facility at the University of Michigan (Vandenheede et al., 2012). The freestream velocity ranges from 5 cm/s to 55 cm/s with a turbulence intensity of about 1%. The channel test cross-section has dimensions 61 cm × 61 cm as shown in Fig. 2, which corresponds to $8c \times 8c$. The model is a stainless-steel flat plate with 7.6 cm chord length spanning the cross-section of the facility. The plate thickness is 4.7 mm and the leading and trailing edges are rounded with radii half the plate thickness. The plate is mounted vertically in the water channel and the immersed span corresponds to $7.6c$, as depicted in Fig. 2a. The distance between the model and the bottom wall of the test section is about 3 mm or $0.04c$. The water channel bottom wall boundary layer thickness at the plate location is around 2.5 cm, approximately three times larger than the gap between the plate and the bottom wall. The two freestream velocities used here are 26 cm/s and 52 cm/s, which correspond to $\mathrm{Re} = 2 \cdot 10^4$ and $4 \cdot 10^4$, respectively. At these flow conditions the water surface does not deform significantly and, therefore, the free surface acts as a symmetry plane suppressing three-dimensional wing tip effects. Similarly the small gap compared to the bottom wall boundary layer thickness minimizes three-dimensional wing tip effects at the bottom wall. It follows that PIV flow measurements at the center plane are not significantly affected by endwall effects, which for unsteady flow phenomena may reach approximately one chord away from the walls (Gardner et al., 2014).

Unsteady velocity fields are obtained through PIV measurements. A double-pulsed Nd-YAG laser (Spectra Physics PIV 300) illuminates a horizontal plane located at $3.7c$ from the channel bottom, i.e. around the mid span of the plate, as shown in Fig. 2a. The water channel is seeded with 3 μm titanium dioxide particles and images are acquired by a digital camera (Cooke Corp. PCO.4000) equipped with Micro-Nikkor 105 mm lens which leads to a magnification of approximately 18 pixels/mm. The maximum acquisition frequency is 1 Hz, which precludes the acquisition of more than one image per period for some of the cases described above.

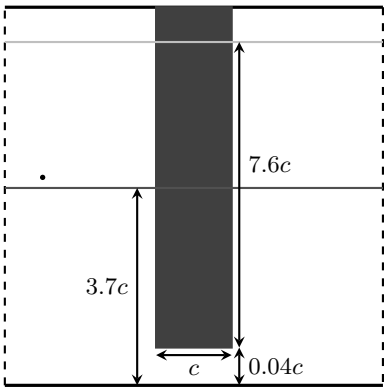

(a) Side view

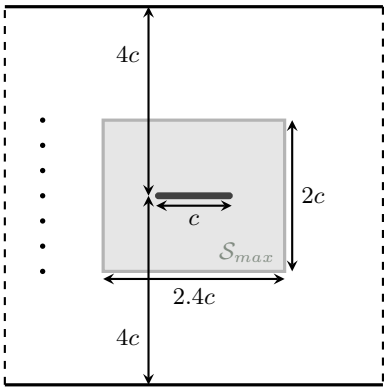

(b) Bottom view

Fig. 2: Schematic views of the plate mounted in the water channel. The seven small discs on the left of the plate represent the location of the dye rake

Images are post-processed by using an in-house code. The particle displacement, and thus the velocity, are determined in multi-passes through cross-correlation analysis. The first low-resolution and second high-resolution passes are performed by using an interrogation window size of 64×64 pixels and 32×32 pixels, respectively. The particle displacement is set to 8 pixels at the freestream velocity. Assuming an accuracy of 0.1 pixel (Raffel et al., 2013), the uncertainty on the velocity is thus 1.25% of the freestream velocity. Two filters are then applied to remove outliers: a median filter based on spatially adjacent values and a $3-\sigma$ filter based on a pre-computed mean and standard deviation at one particular point. After post-processing, PIV fields are obtained on a cartesian grid with a spacing of $c/85$ from which a window $\mathcal{S}_{max}$ of size $2.4c \times 2c$ is extracted. This window, shown in Fig. 2b, corresponds to the largest window on which the indirect calculation of loads can be applied.

For the second test case, a series of 200 snapshots are taken at a frequency lower than the shedding frequency. As these images do not correspond to a specific phase, the velocity field is averaged to obtain the mean flow, as explained above. For the first and third cases, the pitching motion is imposed by a rotary stage (Velmex B4872TS Rotary Table) with an accuracy of 0.0125°. The laser pulses are then synchronized with the kinematics in order to acquire data at a specific phase for phase-averaging. Two hundreds PIV images are collected for one given phase. The experiment is then repeated for subsequent values of the phase, up to a total of 20 phases uniformly distributed within the period of oscillation. A convergence study on the number of snapshots can be found in App. B.

As previously mentioned, part of the flow around the plate lies in the shadow region. To obtain the velocity field in that area, the experiment is repeated with the plate mounted symmetrically with respect to the freestream direction. For the first case, it has been verified that the symmetrical pitching motion leads to a symmetrical flow with respect to the freestream direction (Godoy-Diana et al., 2008). Therefore, the information on one side of the plate is sufficient. The complete velocity field at a specific plate incidence α is thus built from two symmetrical configurations: one with $\alpha > 0$ to measure the velocity field above the plate and another $\alpha < 0$ to obtain the velocity field below it. Since data are missing in the shadow area only, regions exist where the velocity field is obtained for the two configurations. These overlap regions are used to align the two sets of results, the horizontal and vertical shifts between them being determined by finding the best match in velocity magnitude. The two sets of results are then stitched together, the velocity field on the overlap regions being a weighted-average of the results obtained for the two incidences.

Dynamic Mode Decomposition is applied as a preprocessing step to the small amplitude pitching case only. In the case of the plate undergoing large oscillations, the time resolution of the PIV fields was not sufficient to allow a useful decomposition. By definition, DMD is applied to unsteady data and is thus not applicable in the context of the static plate since only the time-averaged velocity is available.

In addition to PIV measurements, loads are measured directly to compare with the indirect calculation. A six-components ATI Mini 40 force/torque transducer mounted on top of the plate is used for that purpose. Expressed in terms of non-dimensional lift, drag and pitching moment coefficients for $\mathrm{Re} = 20\,000$, the sensor resolution is $1.3 \cdot 10^{-2}$ and $4.3 \cdot 10^{-3}$ for forces and pitching moment, respectively. For $\mathrm{Re} = 40\,000$, these values are four times lower. The aerodynamic loads are obtained by subtracting from the sensor output structural static and dynamic loads due to gravity and inertia of the model, respectively. Mea-

sured forces and moments are filtered with a cutoff frequency of 10 Hz and time or phase-averaged. Forces and moments coefficients are non-dimensionalized, respectively, by $1/2\rho U_\infty^2 c l_w$ and $1/2\rho U_\infty^2 c^2 l_w$, where l_w is the length of the plate under water. The moment is measured referenced to the pitching axis and plate center for the pitching and steady state cases, respectively. The pitching moment coefficient about the plate center is calculated *a posteriori*. The direct load measurements results include endwall effects at the water surface and at the channel's bottom wall. These effects are small and the results agree well with data reported in the literature for two-dimensional steady and unsteady conditions (Fage and Johansen, 1927; Granlund et al., 2013).

Finally, dye visualization is used to obtain a qualitative overview of the flow. The apparatus consists of a dye rake made of seven horizontal dye streams that are uniformly distributed over a distance of $2c$, as shown in Fig. 2b. The corresponding streaklines are used to identify three-dimensional effects, as discussed in Sect. 4.4.

4 Results

The two indirect load calculation methods are applied to the different cases described in Sect. 3.1 to calculate the corresponding lift, drag and pitching moment coefficients, the latter being calculated about the half-chord point. First, in Sect. 4.1, parameters appearing in both methodologies are varied and their impacts are studied in the context of the large amplitude pitching case. Then, a particular set is chosen, and the accuracy of the INSE and NOCA methods are compared for the three test cases. The results are presented in Sects. 4.2, 4.3 and 4.4.

4.1 Impact of parameters

The large pitching amplitude case is used first to study the impact of user-defined parameters. This includes the choice of the origin for the location vector x_i in the NOCA method, the control surface $\mathcal{S}$ required to apply both formulations, and the threshold value $I_2^{\mathtt{thres}}$ for the pressure correction in the INSE methodology. The pressure contribution to the loads has been shown to be sensitive to the choice of parameters (Jardin et al., 2009; David et al., 2009; Gharali and Johnson, 2014). The same conclusions are drawn in the present work, whether the pressure calculation is performed directly for INSE, or through $\overline{\gamma}^{Fp}$ and $\overline{\gamma}^{Mp}$ for NOCA.

To highlight the effect of $\mathcal{S}$, the three control surfaces depicted in Fig. 3 and differing by the location x^d of their downstream edge B-C (see Fig. 1) are chosen. The maximal value of x^d is limited by the available PIV window $\mathcal{S}_{max}$ (see Fig. 2b). Moreover, it is known that the estimated loads given by the indirect formulations applied on two adjacent contours $\mathcal{C}_\infty$ can vary significantly. In order to limit that effect, the aerodynamic coefficients obtained in this work are presented in terms of statistics of the non-dimensional loads calculated on several contours. More specifically, each of the three control surfaces differing by their x^d is associated to a further twelve surfaces that are up to $0.15c$ narrower, as illustrated in Fig. 3 by the shaded zones. The aerodynamic coefficients presented for the surfaces defined by $x^d = 0.8c$, c and $1.2c$ are thus calculated by ensemble averaging the results obtained with the corresponding thirteen control surfaces. In addition, the standard deviation associated with these different surfaces is presented as it measures the sensitivity of the results to $\mathcal{S}$. Additionally, as depicted by the dark small discs appearing in Fig. 3, the location of the origin defining x_i in the NOCA method is set at the middle of the shaded zones. To demonstrate the influence of this parameter, results are also compared to those obtained with two other origin locations, as depicted by the white small discs in Fig. 3. Finally, the impact of $I_2^{\mathtt{thres}}$ is investigated by varying $I_2^{\mathtt{thres}}$ using the values 0, 0.025, 0.05 and 0.1.

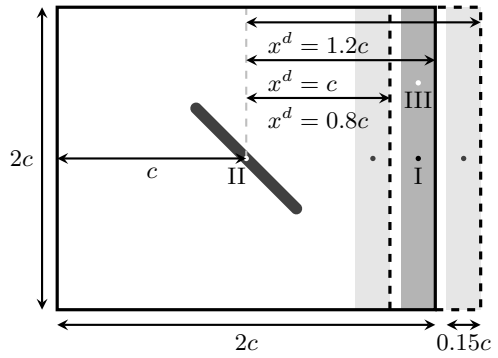

Fig. 3: Schematic view of the location of the control surfaces with respect to the plate. The solid lines define the border of the main contour chosen to compare the indirect methods and the dashed lines denote the additional main contours used in the parameter study. The small discs denoted I, II and III represent the locations considered for the origin in the NOCA method

Although the results obtained by the NOCA method should be independent of the choice of the origin, they depend quite strongly on it in practice. This impact is illustrated by the calculation of lift and drag for the large amplitude pitching motion. Figure 4 shows the coefficient time responses calculated for three different

origin positions (numbered I to III in Fig. 3) and compares them to the direct load measurements. For both lift (Fig. 4a) and drag (Fig. 4b), placing the origin in the wake (I or III) leads to results less noisy than those obtained when the origin lies on the center of the plate (II). Moreover, location III leads to a reduction of the first jump in drag and an increase in the amplitude of the second one compared to location I. Note that a vortex core is located near point III at the phase corresponding to the first jump (see Sect. 4.2). Assuming that the largest errors occur in the wake region where vorticity is large, these results indicate that the contribution from this region is smaller when the distance $\|\mathbf{x}\|$ in Eqs. (7) and (12) is small. Having an origin in the critical region thus reduces the overall error and provides a better estimation of the loads. Consequently, it should be possible to further improve the NOCA results by adapting the location of the origin of $\mathbf{x}$ to the flow topology.

The effects of the size and location of $\mathcal{S}$ for the INSE approach have been previously studied. In particular, David et al. (2009) and Gharali and Johnson (2014) demonstrated that the load coefficients are not very sensitive to the location of edges A-B, C-D and D-E (see Fig. 1 for the definition) as long as they are located outside high vorticity regions. The same authors also showed that only the drag coefficient is very sensitive to the location of the downstream boundary B-C, the variation of results increasing when a vortex center is close to this edge. The weak impact of the upper, lower and upstream edges is also observed in the present work (results left for conciseness). To decrease the sensitivity of the drag to the downstream boundary, Gharali and Johnson (2014) proposed to increase the size of the PIV window in order to find a location for the downstream boundary far from vortical structures. However, the resulting decrease in spatial resolution becomes problematic when the reduced frequency is $k > 0.05$. In the present case, such a large field of view is not achievable and edge B-C has to be located in a region of high vorticity. Figure 5 shows the lift and drag coefficients computed with the INSE method by using the three different control surfaces defined in Fig. 3. In all cases, the pressure correction is applied to the entire edge B-C (i.e., $\Gamma_2^{\texttt{thres}} = 0$). The insensitivity of the lift to the downstream boundary is demonstrated in Fig. 5a. Figure 5b indicates that having the edge B-C closer to the body improves the results as the discontinuous jumps observed between $3T/8$ and $T/2$, and between $7T/8$ and T are in this case much smaller. The same optimal location was reported by David et al. (2009) who suggested that it minimizes the error propagation in the pressure calculation step. However, this proposed explanation does not apply in our case because the pressure correction technique is different. Finally, additional studies of the present data (left out for conciseness) demonstrate that the edge B-C cannot be located too close to the body because the sensitivity to a small change in the surface location increases in this case. Note that the same behavior is observed for the NOCA method.

For the INSE method, the amplitude of the jumps observed in Fig. 5b can be decreased by applying the linear correction of pressure only in the region of large-scale vorticity (edge B′-C′ in Fig 1) as defined by $\Gamma_2^{\texttt{thres}}$. Varying $\Gamma_2^{\texttt{thres}}$ and $\mathcal{S}$, it is found that applying the correction only on a portion of edge B-C decreases the height of the discontinuous jumps in the drag response. This effect can be visualized by comparing results shown in Fig. 5b to those in Fig. 6b where $\Gamma_2^{\texttt{thres}}$ has been set to 0.05. The systematic analysis of this impact reveals that a trade-off between the border location x^d and the threshold $\Gamma_2^{\texttt{thres}}$ should be made to minimize the amplitude of oscillations: the farther away from the plate the border B-C lies, the higher $\Gamma_2^{\texttt{thres}}$ should be.

Based on these findings, the following results have been obtained using a control surface of $2c \times 2c$, $\Gamma_2^{\texttt{thres}} = 0.05$ and the origin located in the wake, at a distance $0.925c$ from the plate center.

4.2 Large amplitude pitching plate

The time response of the load coefficients during a complete cycle of the large amplitude motion with the pivot axis located at the plate center are shown in Fig. 6 and compare rather well with results obtained by direct measurements. In particular, the loads are very well estimated during the middle stages of the upstroke and downstroke, i.e. during the growth of the leading edge vortex, but their amplitudes are underestimated for other parts of the cycle, i.e. when the plate is stalled. Similar results were obtained by Gharali and Johnson (2014). Both the drag and moment coefficients show discontinuous jumps, whose amplitudes depend on the method and the chosen parameter values. Note that the symmetric stitching of PIV fields is clearly visible in the time evolution of the coefficients. The results obtained for the two other pivot locations are not depicted here but exhibit a similar behavior with a better accuracy in load response amplitudes. Note that for these cases, the last term in Eq. (6) contributes to the lift coefficient. However, this contribution corresponds to less than 0.3% of the maximum lift and the impact of the body motion can then be considered as negligible.

As previously discussed, the lack of accuracy visible in Fig. 6 can be linked to vortex shedding and the impact of vortices on the integration path in the

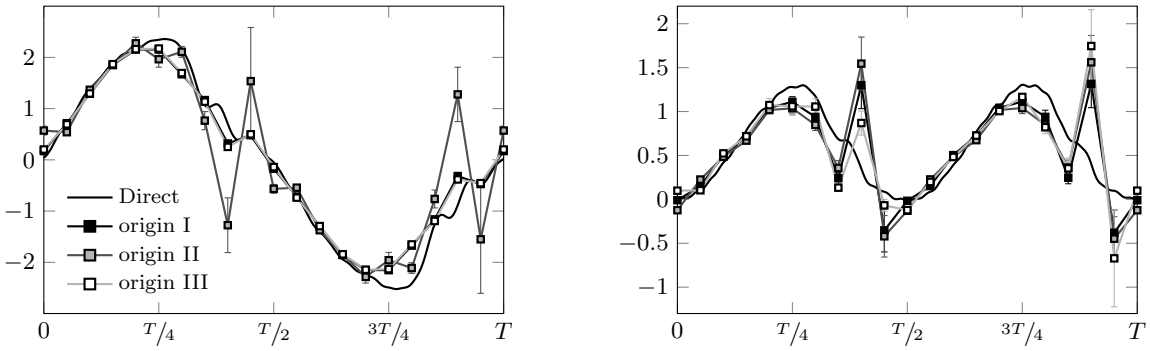

(a) c_l (b) c_d

Fig. 4: Impact of the origin defining the location vector $\mathbf{x}$ on the evolution of the lift and drag coefficients within a pitching period T for large amplitude plate oscillations about a pivot axis at the plate center: indirect calculations using NOCA with different origin locations (symbols) and direct measurements (thick continuous line). The error bars correspond to the sensitivity of the results to the control surface used in the indirect methods

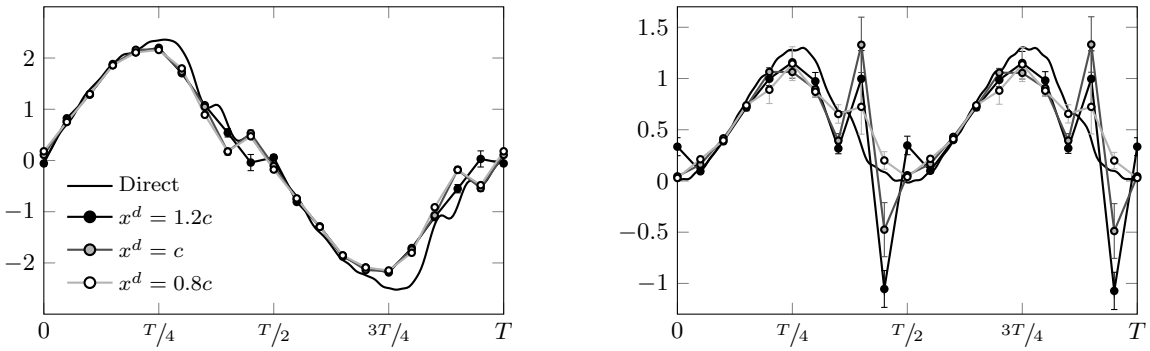

(a) c_l (b) c_d

Fig. 5: Impact of the control surface location on the evolution of the lift and drag coefficients within a pitching period T for large amplitude plate oscillations about a pivot axis at the plate center: indirect calculations using INSE with $\Gamma_2^{\texttt{thres}} = 0$ and different edge B-C positions (symbols) and direct measurements (thick continuous line). The error bars correspond to the sensitivity of the results to the control surface used in the indirect methods

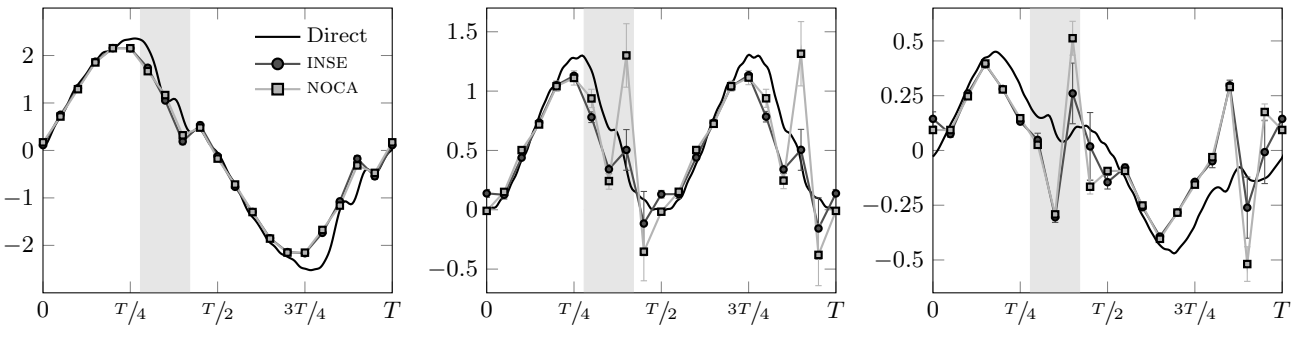

(a) c_l (b) c_d (c) c_m

Fig. 6: Evolution of aerodynamic coefficients within a pitching period T for large amplitude plate oscillations about a pivot axis at the plate center: indirect calculations (symbols) and direct measurements (thick continuous line). The error bars correspond to the sensitivity of the results to the control surface used in the indirect methods

wake, i.e. edge B-C in Fig. 1. Figure 7 shows the velocity and vorticity fields at phases corresponding to the beginning of the downstroke (shaded area in Fig. 6). The field of view of the snapshots in Fig. 7 corresponds to the control surface $\mathcal{S}$. The large leading edge vortex still located near the plate in Fig. 7a is convected downstream and crosses the right edge of Figs. 7b and 7c, which corresponds to the integration path in the wake. The comparison of aerodynamic coefficients response in the gray parts of Fig. 6 with the flow fields depicted in Fig. 7 shows that the accuracy of the load estimation decreases with the increase of flow disturbance on the downstream edge of $\mathcal{S}$ (see Fig. 7a), a jump in the estimation appearing when vortices cross this edge (see Fig. 7b and 7c). The increased measurement noise associated with high vorticity regions probably induces an increase of numerical errors and finally a less accurate estimation of load responses.

Time-averaged and root-mean-square (RMS) statistics of the aerodynamic coefficients are summarized in Tab. 1 and should be analyzed in light of Fig. 6. The mean lift and moment coefficients are both close to zero. This result is expected as the pitching motion is symmetric with respect to the freestream but also because two velocity fields distant in time by half a cycle are built from the same PIV snapshots, as explained in Sect. 3.2. The mean and RMS of the drag coefficient are generally lower than expected because of the underestimation of their response amplitude. Similarly, the RMS value of the lift coefficient estimated by both indirect methods is slightly lower than the direct measurements. Finally, the RMS value of the moment coefficient is artificially improved by the presence of the jumps in its time response.

In conclusion, both indirect methods are able to estimate reasonably well the aerodynamic coefficients of a flat plate undergoing large amplitude pitching motion, the NOCA method being more sensitive to noise even if the user-defined parameters are carefully chosen. However, the estimated load responses must be considered with caution for detached flows especially when a vortex crosses the downstream edge of the control surface.

	Pivot at leading edge					
	$\overline{c_l}$	c_l^{rms}	$\overline{c_d}$	c_d^{rms}	$\overline{c_m}$	c_m^{rms}
INSE	0.03	1.45	0.48	0.64	0.00	0.40
NOCA	0.03	1.45	0.50	0.65	0.00	0.37
Direct	−0.01	1.57	0.54	0.68	−0.01	0.24
	Pivot at center					
	$\overline{c_l}$	c_l^{rms}	$\overline{c_d}$	c_d^{rms}	$\overline{c_m}$	c_m^{rms}
INSE	0.01	1.36	0.49	0.63	0.01	0.22
NOCA	0.01	1.36	0.54	0.75	0.00	0.26
Direct	−0.05	1.56	0.60	0.75	−0.01	0.25
	Pivot at trailing edge					
	$\overline{c_l}$	c_l^{rms}	$\overline{c_d}$	c_d^{rms}	$\overline{c_m}$	c_m^{rms}
INSE	−0.02	1.35	0.57	0.68	0.01	0.27
NOCA	−0.01	1.36	0.61	0.77	0.01	0.23
Direct	−0.02	1.55	0.58	0.74	0.00	0.22

Table 1: Mean and RMS values of aerodynamic coefficients for large amplitude plate oscillations around different pivot axes at $\mathrm{Re} = 2 \cdot 10^4$ computed with the indirect methods and obtained from direct measurements

	Angle of attack 30°		
	$\overline{c_l}$	$\overline{c_d}$	$\overline{c_m}$
INSE	1.00 ± 0.00	0.56 ± 0.04	0.12 ± 0.01
NOCA	1.00 ± 0.00	0.57 ± 0.04	0.12 ± 0.01
Direct	0.99	0.63	0.12
	Angle of attack 45°		
	$\overline{c_l}$	$\overline{c_d}$	$\overline{c_m}$
INSE	1.00 ± 0.01	1.12 ± 0.07	0.15 ± 0.01
NOCA	0.99 ± 0.02	1.13 ± 0.07	0.16 ± 0.02
Direct	1.01	1.09	0.12

Table 2: Mean values of aerodynamic coefficients for static plate at 30° and 45° at $\mathrm{Re} = 4 \cdot 10^4$ computed with the indirect methods and obtained from direct measurements. The standard deviations indicated for the indirect calculation represent the sensitivity of the results to the choice of control surface $\mathcal{S}$

4.3 Static plate

The mean load coefficients calculated for the static plate by using indirect methods are shown in Tab. 2, together with the mean results obtained from direct measurements. Note that, due to the time-averaging used in this case, the major contribution to the term $\overline{u_i' u_j'}$ stems from the unsteady flow dynamics (i.e., vortex shedding) and not from the turbulence itself. As described above, the standard deviation is computed from the results obtained by using different control surfaces $\mathcal{S}$.

Albrecht et al. (2013) studied a similar flow by using the INSE and NOCA approaches. Their results were shown to be highly sensitive to the choice of indirect approach. They concluded that NOCA should be used for the lift, while INSE provides better results for the drag. Moreover, a high sensitivity to the location of $\mathcal{S}$ was reported. The present work leads to different conclusions. First, the results show that the two indirect methodologies can provide a reasonably good estimation of the mean aerodynamic coefficients for both angles of attack. In particular, the lift is predicted with a maximal relative error of about 2%. The relative error on the mean drag coefficient is higher for both method-

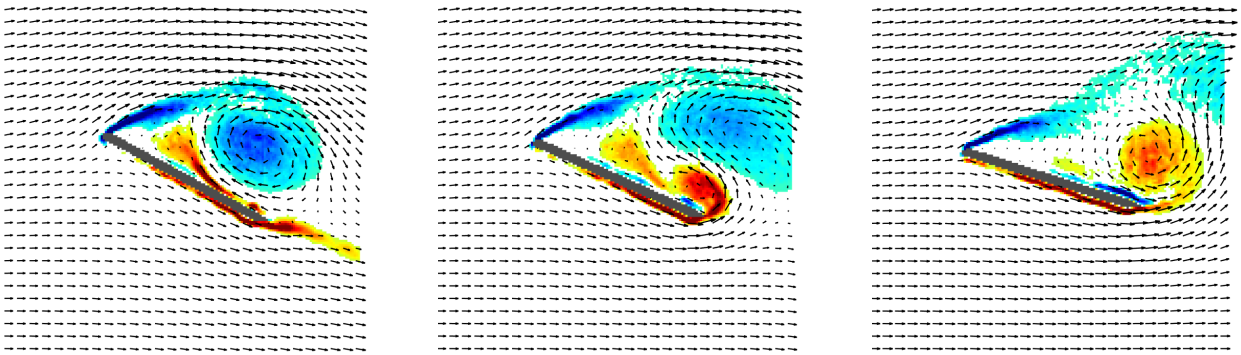

(a) $0.31T$ and $\alpha = 28.2°$ (b) $0.36T$ and $\alpha = 23.6°$ (c) $0.41T$ and $\alpha = 16.6°$

Fig. 7: Phase-averaged PIV velocity and vorticity fields at three phases in the downstroke of the large amplitude pitching cycle. The red and blue fields correspond, respectively, to positive and negative vorticity, i.e. counter-clockwise and clockwise vortices. The field of view corresponds to the surface of reference for INSE and NOCA methods

ologies with a maximum of 13% at an angle of attack of 30°. The highest relative error is found to be 25% for the pitching moment at an angle of attack of 45°. However, it should be considered in light of the relatively small average value of this coefficient. Finally, the sensitivity to the control surface is low and similar for the two methods, as shown by the low standard deviations.

	Angle of attack					
	$30° \pm 0.77°$			$45° \pm 1.33°$		
	$\overline{c_l}$	$\overline{c_d}$	$\overline{c_m}$	$\overline{c_l}$	$\overline{c_d}$	$\overline{c_m}$
INSE	1.15	0.66	0.10	1.10	1.12	0.10
NOCA	1.15	0.68	0.11	1.09	1.11	0.10
Direct	1.08	0.69	0.13	1.07	1.15	0.12

Table 3: Mean values of aerodynamic coefficients for small amplitude plate oscillations around a mean angle of attack of 30° and 45° at $\mathrm{Re} = 4 \cdot 10^4$ computed with the indirect methods and obtained from direct measurements. Results are shown for the original data (without DMD)

4.4 Small amplitude pitching plate

The methods are now applied to the small amplitude pitching cases. The response of the phase-averaged lift and drag coefficients during a pitching cycle is shown in Figs. 8a and 8b for an angle of attack of 30°. Results for an incidence of 45° are not shown here but exhibit similar behavior and the same conclusions can be drawn. Table 3 shows the mean lift, drag and pitching moment coefficients. The comparison of results obtained by direct measurements for the static and the small amplitude pitching plate (see Tabs. 2 and 3) shows that the imposed motion does not significantly impact the flow dynamics since the relative difference between the mean coefficients is below 10%.

As shown in Figs. 8a and 8b, the responses of the estimated lift and drag coefficients are very noisy. Only global trends can be seen for the lift coefficient computed by both the NOCA and INSE methods, the noise in the drag response is even higher, to the point where only the mean drag has a meaningful value. The moment response is not shown here but is very similar to that of the drag. Additionally, the large error bars indicate a strong sensitivity of the results to the choice of the control surface. However, despite the noise in the load responses, the mean coefficients are well approximated, as shown in Tab. 3.

As shown by David et al. (2009), these unsatisfactory responses can be partially explained by three-dimensional effects caused by the massive flow separation. Figure 9 shows pictures acquired with dye visualization. As the snapshots consist in side views of the plate, they depict flow in the chordwise and spanwise directions and can demonstrate the existence of three-dimensional effects. Three plate configurations are considered: the plate is first aligned with the flow (see Fig. 9a) and then small and large amplitude pitching motions are imposed (see Figs. 9b and 9c). While the flow is clearly two-dimensional at zero incidence (see Fig. 9a), important three-dimensional structures are observed for the small amplitude case (see Fig. 9b). Moreover, the flow varies strongly from one shedding period to the next and the shedding frequency fluctuates slightly in time, as clearly observed in flow visualization movies and direct measurements. The lack of

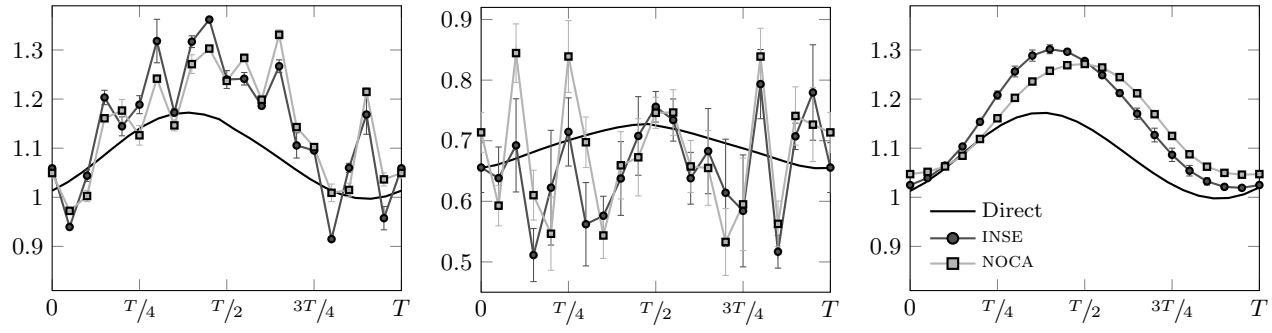

(a) c_l (without DMD) (b) c_d (without DMD) (c) c_l (with DMD)

Fig. 8: Evolution of lift and drag coefficients within a pitching period T for small amplitude plate oscillations around a mean angle of attack of 30° with and without DMD pre-processing: indirect calculation (symbols) and direct measurements (thick continuous line). The error bars correspond to the sensitivity of the results to the control surface used in the indirect method

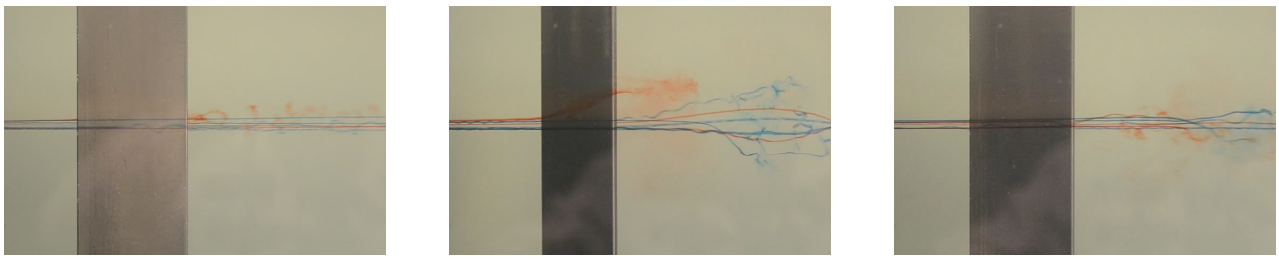

(a) Static at 0° (b) Small pitching motion around 45° (c) Large pitching motion around 0°

Fig. 9: Dye visualization for three cases similar to the ones considered in this study at $\mathrm{Re} = 1.8 \cdot 10^4$. Side view: the flow is from left to right and the darker region corresponds to the plate

coherence between the snapshots induces noise in the ensuing averaged PIV fields. As a consequence, the two sets of data for the top and bottom sides of the plate do not match well in the overlapping regions, introducing additional noise in the velocity field during the stitching phase. These different noise contributions can explain why the application of INSE and NOCA methods leads to the unsatisfactory results depicted in Figs. 8a and 8b. A convergence study has been performed on the number of snapshots that are averaged to compute the PIV flow fields at each phase. The results shown in App. B demonstrate that increasing the number of snapshots decreases the noise in the estimated time responses of coefficients. Therefore, it would be possible to further improve the results by acquiring a higher number of PIV images at each phase. Finally, as shown in Fig. 9c, the flow is much more two-dimensional for the large amplitude case, the coherence of the flow along the span being enforced by a more energetic pitching motion. This explains why better load responses are obtained in this case.

In order to reduce the noise in the velocity field, the phase-averaged fields are pre-processed, i.e. filtered by DMD, where only the first three modes are retained to approximate the original fields. These modes are chosen as explained in Sect. 2.3 and correspond to the mean flow, the shedding/pitching frequency and its first harmonic. This pre-processing step leads to smoother responses, as shown in Fig. 8c for the lift coefficient. However, several discrepancies remain, such as the extrema obtained with the NOCA method that seem to be slightly shifted in phase compared to the direct measurements. Note that this shift can also be observed in Fig. 8a, i.e. without the filtering step. Finally, the DMD pre-processing improves results for lift but not for drag and moment coefficients (not shown here), the noise in the PIV fields being too high to determine the frequency content of their responses.

5 Conclusions

Two indirect methods based on momentum balance applied to a control surface surrounding a body have been applied to estimate the aerodynamic forces and pitching moment from 2D-PIV measurements. The first

approach uses directly the integral formulation of the Navier-Stokes equations, while the second is based on the so-called "flux equation", proposed by Noca et al. (1999) for the estimation of forces and extended here to the calculation of moments. These indirect formulations have been applied to three different unsteady flows around a plate: large amplitude pitching around 0°, static at high angle of attack and small amplitude pitching around a high angle of attack. In order to assess the quality of the indirect calculations, the results have also been compared to direct load measurements.

It has been shown that the mean loads can be estimated with satisfactory accuracy for both static and dynamic cases, by using either indirect methodology. However, the time response of unsteady coefficients is more difficult to capture and the accuracy of the estimation varies with the type of flow considered. As previously shown by David et al. (2009) and Gharali and Johnson (2014), the level of noise in spatio-temporal data impacts the calculation through the estimation of the pressure contribution to the total loads and can result in inaccurate load time responses. These problems are more pronounced in the case of a small amplitude pitching motion around a high angle of attack, for which the flow is found to be more three-dimensional and less periodic. In this case, increasing the number of PIV snapshots acquired at each phase would help to improve the indirect estimation of load responses. The time response is better captured in the case of large amplitude pitching motion since the strong structural forcing induces better spatial and temporal coherence of the flow. In that context, both indirect methodologies perform very well as long as there is no vortical structure close to the downstream boundary. As reported by Gharali and Johnson (2014), discrepancies in the amplitude of the estimated load coefficient responses appear when there are large vortices crossing the boundary of integration.

The noise in PIV measurements additionally causes a sensitivity of the results to the choice of the different user-defined parameters required for both formulations. The impact of these parameters has been highlighted and guidelines for setting their values have been proposed. Moreover, it has been shown that the noise sensitivity can be reduced through the use of DMD (or other filtering methods) as a pre-processing step, as long as the information is present in the PIV fields. This procedure filters part of the noise and leads to a smoother load response while retaining the main features of the flow dynamics. It has been applied to a plate pitching with small amplitude around a high mean angle and led to an improvement in the estimated lift response. Nonetheless, discrepancies with direct measurements still remain, as filtering cannot correct errors existing in velocity field or compensate for the limited spatial and temporal resolution of the original PIV data.

Further efforts will be directed to improvement in the estimation of the pressure contribution to the total loads, which has a major impact on the result accuracy. For both methods, such improvement could be achieved through the adaptation of user-defined parameters to the topology of the flow.

Acknowledgements Experimental research conducted at the University of Michigan was sponsored in part by the Air Force Office of Scientific Research's Multidisciplinary University Research Initiative (MURI), contract number FA9550-07-1-0547, Dr. Doug Smith program monitor, and by the Michigan/AFRL Collaborative Center in Aeronautical Sciences.

A Extension of the "flux equation" to the calculation of moments

It is possible to extend "flux equation" proposed by Noca et al. (1999) to the calculation of aerodynamic moments about an arbitrary defined origin. Assumed negative according to the right-hand rule, the moments can be calculated by using

$$\begin{aligned}\mathbf{M} = &\oint_{\mathcal{S}_\infty+\mathcal{S}_b} \mathbf{n}\cdot\boldsymbol{\gamma}^{Mt}\,\mathrm{d}\mathcal{S} - \oint_{\mathcal{S}_b}\Big(\mathbf{u}^b\cdot\mathbf{n}\Big)\,(\rho\mathbf{u}\times\mathbf{x})\,\mathrm{d}\mathcal{S}\\ &+\oint_{\mathcal{S}_\infty}\mathbf{n}\cdot\boldsymbol{\gamma}^{Mp}\,\mathrm{d}\mathcal{S} - \oint_{\mathcal{S}_\infty}\mathbf{n}\cdot([\rho\mathbf{u}\mathbf{u}-\boldsymbol{\tau}]\times\mathbf{x})\,\mathrm{d}\mathcal{S},\end{aligned} \tag{14}$$

with

$$\begin{aligned}\boldsymbol{\gamma}^{Mt} = &-\frac{\rho}{2}\|\mathbf{x}\|^2\,\partial_t\mathbf{u}\times\mathbf{I} + \rho\,(\mathbf{u}\times\mathbf{x})\,\mathbf{u}\\ &+\frac{\rho}{2}\|\mathbf{x}\|^2\,\mathbf{u}\boldsymbol{\omega} - \frac{\rho}{2}\|\mathbf{x}\|^2\,\boldsymbol{\omega}\mathbf{u}\\ &-\frac{\rho}{2}\|\mathbf{u}\|^2\,\mathbf{x}\times\mathbf{I} + \rho\,([\mathbf{u}\mathbf{u}]\cdot\mathbf{x})\times\mathbf{I}\\ &+\mu\mathbf{x}\boldsymbol{\omega} + \mu\mathcal{N}\mathbf{u}\times\mathbf{I} - \frac{\mu}{2}\|\mathbf{x}\|^2\nabla\boldsymbol{\omega},\end{aligned} \tag{15}$$

and

$$\begin{aligned}\boldsymbol{\gamma}^{Mp} = &-\frac{\rho}{2}\,\|\mathbf{u}\|^2\,(\mathbf{x}\times\mathbf{I})\\ &-\frac{\rho}{\mathcal{N}}\,([\partial_t\mathbf{u}\times\mathbf{I}]\cdot\mathbf{x})\,\mathbf{x} + \frac{\rho}{\mathcal{N}}\|\mathbf{x}\|^2\,(\partial_t\mathbf{u}\times\mathbf{I})\\ &+\frac{\rho}{\mathcal{N}}\,([\{\mathbf{u}\times\boldsymbol{\omega}\}\times\mathbf{I}]\cdot\mathbf{x})\,\mathbf{x} - \frac{\rho}{\mathcal{N}}\|\mathbf{x}\|^2\,(\{\mathbf{u}\times\boldsymbol{\omega}\}\times\mathbf{I})\\ &+\frac{1}{\mathcal{N}}\,([\{\nabla\cdot\boldsymbol{\tau}\}\times\mathbf{I}]\cdot\mathbf{x})\,\mathbf{x} - \frac{1}{\mathcal{N}}\|\mathbf{x}\|^2\,(\{\nabla\cdot\boldsymbol{\tau}\}\times\mathbf{I}),\end{aligned} \tag{16}$$

where $\mathbf{x}$ is a location vector with respect the origin, $\mathbf{u}^b$ is the body velocity and $\mathcal{N}$ the number of dimensions. Note that for the sake of concision, only instantaneous quantities are considered. Statistical mean quantities can be retrieved by averaging equations and by using the Reynolds decomposition. The derivation of Eqs. (14)-(16) is similar to what was done by Noca et al. (1999) for the calculation of forces. Starting from the integral Navier-Stokes equations, the moments can be expressed as

$$\mathbf{M} = -\mathrm{d}_t\int_{\mathcal{V}}\rho\mathbf{u}\times\mathbf{r}\,\mathrm{d}\mathcal{V} - \oint_{\mathcal{S}_\infty}(\mathbf{n}\cdot[p\mathbf{I}+\rho\mathbf{u}\mathbf{u}-\boldsymbol{\tau}])\times\mathbf{r}\,\mathrm{d}\mathcal{S}, \tag{17}$$

where $\mathbf{r}$ is the location vector with respect to the point R about which the moment is calculated. The derivation is then done in two steps, first the elimination of pressure and then the rewriting of volume integral into surface integrals. Note that it is assumed here that the external surface $\mathcal{S}_\infty$ is static and that there is no flow through the body surface.

A.1 Elimination of pressure

To rewrite the pressure, Noca et al. (1999) uses the so-called Pressure identity. However, it cannot be directly used for the calculation of moments. Instead, the pressure term can be rewritten by using the Extended Pressure identity, derived from the Pressure identity and defined as

$$-\oint_{\mathcal{S}} \phi\,(\mathbf{n}\times\mathbf{x})\;\mathrm{d}\mathcal{S} = \frac{1}{\mathcal{N}}\oint_{\mathcal{S}} \mathbf{x}\times[\mathbf{x}\times(\nabla\phi\times\mathbf{n})]\;\mathrm{d}\mathcal{S}, \tag{18}$$

where $\mathbf{x}$ is a location vector, $\mathcal{N}$ the dimension of space, ϕ an arbitrary scalar and $\mathbf{n}$ the unit normal to the surface $\mathcal{S}$. Note that the domain enclosed by $\mathcal{S}$ can be multiply-connected.

The pressure term can be rewritten by assuming $\mathbf{r}=\mathbf{x}$ and by using Eq. (18) with $\phi = p$. Moreover, the pressure gradient can be expressed as a function of the velocity field by using the differential form of the Navier-Stokes equations

$$\nabla p = -\rho\partial_t\mathbf{u} - \nabla(\frac{\rho}{2}\|\mathbf{u}\|^2) + \rho\mathbf{u}\times\boldsymbol{\omega} + \nabla\cdot\boldsymbol{\tau}. \tag{19}$$

Finally, by using the vector identity

$$\mathbf{x}\times(\mathbf{x}\times[\mathbf{a}\times\mathbf{n}]) = \mathbf{n}\cdot\left(\{[\mathbf{a}\times\mathbf{I}]\cdot\mathbf{x}\}\,\mathbf{x} - \|\mathbf{x}\|^2\,[\mathbf{a}\times\mathbf{I}]\right), \tag{20}$$

the pressure term can be written as

$$-\oint_{\mathcal{S}_\infty} p\,(\mathbf{n}\times\mathbf{x})\;\mathrm{d}\mathcal{S} = \oint_{\mathcal{S}_\infty} \mathbf{n}\cdot\boldsymbol{\gamma}^{Mp}\,\mathrm{d}\mathcal{S}, \tag{21}$$

where $\boldsymbol{\gamma}^{Mp}$ is given by Eq. (16). Note that if $\mathcal{N}=2$, the first term on the right-hand side of Eq. (20) vanishes, leading to simplification in Eq. (16).

A.2 Elimination of volume integral

The volume integral appearing in Eq. (17) can be first rewritten by using the Reynolds transport theorem. Thus, by considering $\mathbf{r}=\mathbf{x}$, this yields to

$$\begin{aligned}-\mathrm{d}_t\int_{\mathcal{V}}\rho\mathbf{u}\times\mathbf{x}\,\mathrm{d}\mathcal{V} = &\int_{\mathcal{V}}\rho\mathbf{x}\times\partial_t\mathbf{u}\,\mathrm{d}\mathcal{V}\\ &-\oint_{\mathcal{S}_b}\left(\mathbf{u}^b\cdot\mathbf{n}\right)(\rho\mathbf{u}\times\mathbf{x})\;\mathrm{d}\mathcal{S},\end{aligned} \tag{22}$$

where $\mathbf{u}^b$ is the body velocity. Then, the quantity $\mathbf{x}\times\partial_t\mathbf{u}$ is rewritten in terms of field derivatives. This is achieved by starting from

$$\mathbf{x}\times\partial_t\mathbf{u} = \frac{1}{2}\nabla\times\left(\|\mathbf{x}\|^2\partial_t\mathbf{u}\right) - \frac{1}{2}\|\mathbf{x}\|^2\partial_t\boldsymbol{\omega}, \tag{23}$$

and by taking advantage of the vorticity equation

$$\partial_t\boldsymbol{\omega} = (\boldsymbol{\omega}\cdot\nabla)\,\mathbf{u} - (\mathbf{u}\cdot\nabla)\,\boldsymbol{\omega} + \nu\nabla^2\boldsymbol{\omega}. \tag{24}$$

Then, the following relations are used

$$\|\mathbf{x}\|^2\,(\mathbf{u}\cdot\nabla)\,\boldsymbol{\omega} = \nabla\cdot\left(\|\mathbf{x}\|^2\mathbf{u}\boldsymbol{\omega}\right) - 2\,(\mathbf{x}\cdot\mathbf{u})\,\boldsymbol{\omega}, \tag{25}$$

$$\|\mathbf{x}\|^2\,(\boldsymbol{\omega}\cdot\nabla)\,\mathbf{u} = \nabla\cdot\left(\|\mathbf{x}\|^2\boldsymbol{\omega}\mathbf{u}\right) - 2\,(\mathbf{x}\cdot\boldsymbol{\omega})\,\mathbf{u}, \tag{26}$$

$$\|\mathbf{x}\|^2\nabla^2\boldsymbol{\omega} = \nabla^2\left(\|\mathbf{x}\|^2\boldsymbol{\omega}\right) - \nabla\cdot(4\mathbf{x}\boldsymbol{\omega}) + 2\mathcal{N}\boldsymbol{\omega}, \tag{27}$$

$$\begin{aligned}(\mathbf{x}\cdot\mathbf{u})\,\boldsymbol{\omega} = &-\nabla\times\left[\frac{1}{2}\|\mathbf{u}\|^2\mathbf{x} - (\mathbf{u}\mathbf{u})\cdot\mathbf{x}\right]\\ &-\nabla\cdot[(\mathbf{u}\times\mathbf{x})\,\mathbf{u}] + (\mathbf{x}\cdot\boldsymbol{\omega})\,\mathbf{u},\end{aligned} \tag{28}$$

to finally obtain

$$\begin{aligned}\mathbf{x}\times\partial_t\mathbf{u} = &\nabla\times\left(\frac{1}{2}\|\mathbf{x}\|^2\partial_t\mathbf{u}\right) + \nabla\cdot\left(\frac{1}{2}\|\mathbf{x}\|^2\mathbf{u}\boldsymbol{\omega}\right)\\ &+\nabla\times\left(\frac{1}{2}\|\mathbf{u}\|^2\mathbf{x} - [\mathbf{u}\mathbf{u}]\cdot\mathbf{x}\right)\\ &+\nabla\cdot([\mathbf{u}\times\mathbf{x}]\,\mathbf{u}) - \nabla\cdot\left(\frac{1}{2}\|\mathbf{x}\|^2\boldsymbol{\omega}\mathbf{u}\right)\\ &-\nabla\cdot\left(\nabla\left[\frac{\nu}{2}\|\mathbf{x}\|^2\boldsymbol{\omega}\right]\right) + \nabla\cdot(2\nu\mathbf{x}\boldsymbol{\omega}) - \nabla\times(\nu\mathcal{N}\mathbf{u}).\end{aligned} \tag{29}$$

At last, the Gauss theorem is used to express the volume integral as a surface integral:

$$\begin{aligned}-\mathrm{d}_t\int_{\mathcal{V}}\rho\mathbf{u}\times\mathbf{x}\,\mathrm{d}\mathcal{V} = &\oint_{\mathcal{S}_\infty+\mathcal{S}_b}\mathbf{n}\cdot\boldsymbol{\gamma}^{Mt}\,\mathrm{d}\mathcal{S}\\ &-\oint_{\mathcal{S}_b}\left(\mathbf{u}^b\cdot\mathbf{n}\right)(\rho\mathbf{u}\times\mathbf{x})\;\mathrm{d}\mathcal{S},\end{aligned} \tag{30}$$

with $\boldsymbol{\gamma}^{Mt}$ given by Eq. (15). Note that if $\mathcal{N}=2$, the vortex stretching term in Eq. (24) vanishes and several terms in Eq. (15) disappear.

B Convergence study on the number of PIV snapshots needed for averaging

The INSE and NOCA methods have been applied to PIV fields obtained by averaging 50, 100, 150 and 200 snapshots, for the three cases investigated here. The results presented below are obtained from the INSE approach but similar conclusions can be drawn for the NOCA methodology.

For the large amplitude pitching plate, it appears that the load responses are very similar for the four numbers of images considered, as depicted in Fig. 10. Moreover, the statistics calculated from each signal are almost the same, with a maximum difference of 4%. Therefore, 50 images would be already enough to obtain a good estimation of the load coefficients. Note that this number differs significantly from the results of Gharali and Johnson (2014) who reported a minimum of 500 images required for a similar case.

For the static plate, the data based on 50 snapshots lead to a reasonable estimation of the mean coefficients. However, 150 images are needed to obtain a sensitivity to the location of $\mathcal{S}$ similar to the results reported in Tab. 2. Note that the number of images required for this case increases compared to the large amplitude pitching case. This is probably because the coherence between snapshots decreases.

For the small amplitude pitching plate case, the mean coefficients are similar whether computed with PIV fields obtained from 50, 100, 150 or 200 images. Nonetheless, it seems that increasing the number of snapshots leads to a decrease of the noise in the coefficient responses, as depicted in Fig. 11. Therefore, it could be expected that a higher number of snapshots could further improve the results.

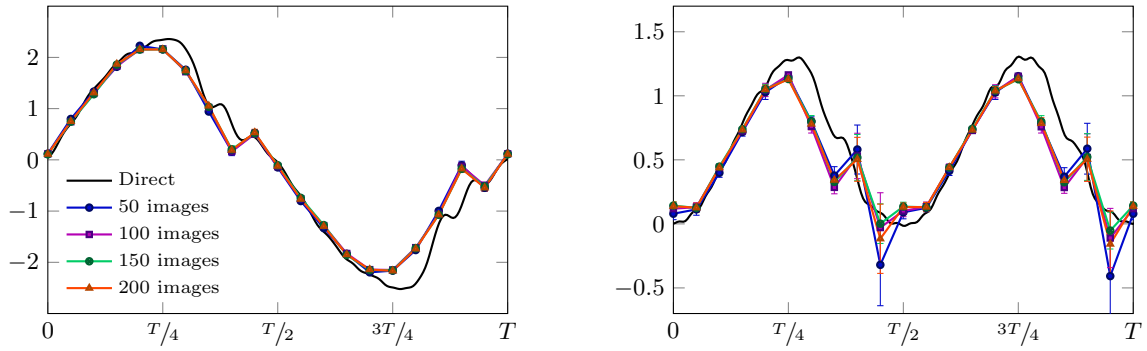

(a) c_l (b) c_d

Fig. 10: Impact of the number of snapshots used on the evolution of lift and drag coefficients within a pitching period T for large amplitude plate oscillations around a mean angle of attack of 0°: indirect calculation using INSE (symbols) and direct measurements (thick continuous line). The error bars correspond to the sensitivity of the results to the control surface used in the indirect method

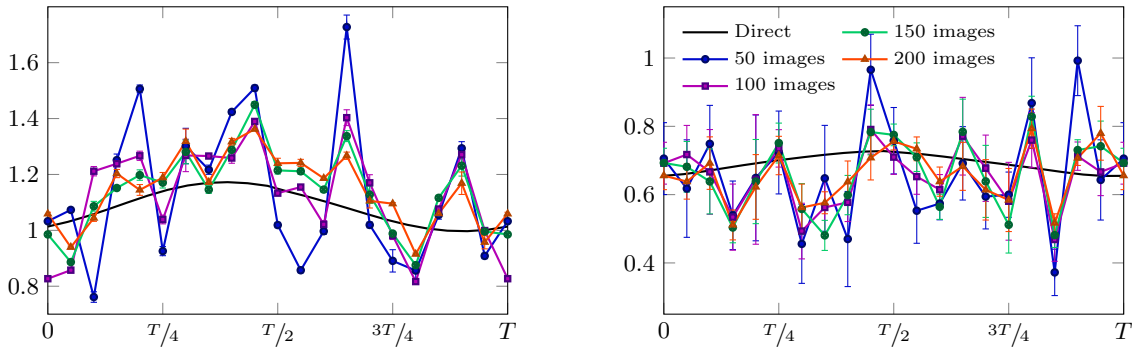

(a) c_l (b) c_d

Fig. 11: Impact of the number of snapshots used on the evolution of lift and drag coefficients within a pitching period T for small amplitude plate oscillations around a mean angle of attack of 30°: indirect calculation using INSE (symbols) and direct measurements (thick continuous line). The error bars correspond to the sensitivity of the results to the control surface used in the indirect method

References

Adrian RJ (1991) Particle-imaging techniques for experimental fluid mechanics. Annual review of fluid mechanics 23(1):261–304

Albrecht T, del Campo V, Weier T, Gerbeth G (2012) Comparison of PIV-based methods for airfoil loads evaluation. In: 16th International Symposium on Applications of Laser Techniques to Fluid Mechanics, Lisbon, Portugal, July, vol 9, p 12

Albrecht T, del Campo V, Weier T, Metzkes H, Stiller J (2013) Deriving forces from 2D velocity field measurements. The European Physical Journal Special Topics 220(1):91–100

Barlow JB, Rae WH, Pope A (1999) Low-Speed Wind Tunnel Testing. John Wiley

Charonko JJ, King CV, Smith BL, Vlachos PP (2010) Assessment of pressure field calculations from particle image velocimetry measurements. Measurement Science and Technology 21(10):105,401

Dabiri JO, Bose S, Gemmell BJ, Colin SP, Costello JH (2014) An algorithm to estimate unsteady and quasi-steady pressure fields from velocity field measurements. Journal of Experimental Biology pp jeb–092,767

David L, Jardin T, Farcy A (2009) On the non-intrusive evaluation of fluid forces with the momentum equation approach. Measurement Science and Technology 20(9):095,401

Fage A, Johansen FC (1927) On the flow of air behind an inclined flat plate of infinite span. Proceedings of the Royal Society of London Series A 116:170–197

Gardner AD, Klein C, Sachs WE, Henne U, Mai H, Richter K (2014) Investigation of three-dimensional dynamic stall on an airfoil using fast-response pressure-sensitive paint. Experiments in Fluids 55(9):1807

Gharali K, Johnson DA (2014) PIV-based load investigation in dynamic stall for different reduced frequencies. Experiments in Fluids 55(8):1803

Godoy-Diana R, Aider JL, Wesfreid JE (2008) Transitions in the wake of a flapping foil. Physical Review E 77(1):016,308

Graftieaux L, Michard M, Grosjean N (2001) Combining PIV, POD and vortex identification algorithms for the study of unsteady turbulent swirling flows. Measurement Science and Technology 12(9):1422

Granlund KO, Ol MV, Bernal LP (2013) Unsteady pitching flat plates. Journal of Fluid Mechanics 733

Gurka R, Liberzon A, Hefetz D, Rubinstein D, Shavit U (1999) Computation of pressure distribution using PIV velocity data. In: Workshop on particle image velocimetry, vol 2

Jardin T, Chatellier L, Farcy A, David L (2009) Correlation between vortex structures and unsteady loads for flapping motion in hover. Experiments in Fluids 47(4-5):655

Jones BM (1936) The measurement of profile drag by the pitot-traverse method. HM Stationery Office

Kurtulus DF, Scarano F, David L (2007) Unsteady aerodynamic forces estimation on a square cylinder by TR-PIV. Experiments in Fluids 42(2):185–196

Lam KM, Leung MYH (2005) Asymmetric vortex shedding flow past an inclined flat plate at high incidence. European Journal of Mechanics - B/Fluids 24(1):33–48

Laskari A, de Kat Rd, Ganapathisubramani B (2016) Full-field pressure from snapshot and time-resolved volumetric PIV. Experiments in Fluids 57(3):44

Lin JC, Rockwell D (1996) Force identification by vorticity fields: techniques based on flow imaging. Journal of Fluids and Structures 10(6):663–668

McLachlan BG, Bell JH (1995) Pressure-sensitive paint in aerodynamic testing. Experimental Thermal and Fluid Science 10(4):470–485

Noca F, Shiels D, Jeon D (1997) Measuring instantaneous fluid dynamic forces on bodies, using only velocity fields and their derivatives. Journal of Fluids and Structures 11(3):345–350

Noca F, Shiels D, Jeon D (1999) A comparison of methods for evaluating time-dependent fluid dynamic forces on bodies, using only velocity fields and their derivatives. Journal of Fluids and Structures 13(5):551–578

van Oudheusden BW (2013) PIV-based pressure measurement. Measurement Science and Technology 24(3):032,001

van Oudheusden BW, Scarano F, Casimiri EWF (2006) Non-intrusive load characterization of an airfoil using PIV. Experiments in Fluids 40(6):988–992

Raffel M, Willert CE, Kompenhans J, et al. (2013) Particle image velocimetry: a practical guide. Springer

Rival D, Prangemeier T, Tropea C (2009) The influence of airfoil kinematics on the formation of leading-edge vortices in bio-inspired flight. Experiments in Fluids 46(5):823–833

Schmid PJ (2010) Dynamic mode decomposition of numerical and experimental data. Journal of Fluid Mechanics 656:5–28

Sterenborg JJHM, Lindeboom RCJ, Simão Ferreira CJ, van Zuijlen AH, Bijl H (2014) Assessment of PIV-based unsteady load determination of an airfoil with actuated flap. Journal of Fluids and Structures 45:79–95

Tan BT, Thompson MC, Hourigan K (2005) Evaluating fluid forces on bluff bodies using partial velocity data. Journal of Fluids and Structures 20(1):5–24

Tropea C, Yarin AL, Foss JF (2007) Springer handbook of experimental fluid mechanics, vol 1. Springer Science & Business Media

Unal M, Lin JC, Rockwell D (1997) Force prediction by PIV imaging: a momentum-based approach. Journal of Fluids and Structures 11(8):965–971

Vandenheede R, Bernal LP, Morrison CL, Humbert S (2012) Parameter space exploration of bio-inspired hover kinematics. In: 42nd AIAA Fluid Dynamics Conference and Exhibit, New Orleans, USA, 25-28 June 2012; AIAA 2012-3155, American Institute of Aeronautics and Astronautics (AIAA)

Villegas A, Diez FJ (2014) On the quasi-instantaneous aerodynamic load and pressure field measurements on turbines by non-intrusive PIV. Renewable Energy 63:181–193